# Comparison of Precipitable Water Vapor Observations by Spaceborne Radar Interferometry and Meteosat 6.7-$\mu$m Radiometry

RAMON F. HANSSEN

*Delft Institute for Earth-Oriented Space Research, Delft University of Technology, Delft, Netherlands*

ARNOUT J. FEIJT

*Royal Netherlands Meteorological Institute, De Bilt, Netherlands*

ROLAND KLEES

*Delft Institute for Earth-Oriented Space Research, Delft University of Technology, Delft, Netherlands*

### ABSTRACT

Satellite radar interferometry (InSAR) can be applied to study vertically integrated atmospheric refractivity variations with a spatial resolution of 20 m and an accuracy of 2 mm, irrespective of cloud cover or solar illumination. The data are derived from the difference between the radar signal delay variations within the imaged area during two acquisitions with a temporal separation of one or more days. Hence, they reflect the superposition of the refractivity distribution during these two acquisitions. On short spatial scales, integrated refractivity variations are dominantly caused by spatial heterogeneities in the water vapor distribution. Validation of the radar interferometric results can be difficult, since conventional imaging radiometers do not provide quantitative measures for water vapor content over the entire tropospheric column and are lacking in spatial resolution. Moreover, comparable quantitative data such as signal delay observed by Global Positioning System (GPS) receivers are only available as time series at a fixed position. In this study, the technique of InSAR-integrated refractivity mapping is discussed and validated for a specific atmospheric situation where brightness temperature variations in Meteosat 6.7-$\mu$m radiometer data could be mapped to precipitable water vapor to validate the InSAR data. The parameterization of the radiometer data is obtained by using a series of 27 hourly GPS signal delay observations at a fixed location and corresponding Meteosat observations at the location of the GPS receiver. Although this methodology for validating the InSAR results is not generally applicable, the results for this specific situation show that the precipitable water vapor observations in both datasets agree to an accuracy of 1.23 kg m$^{-2}$, supporting the interpretation of the InSAR data in terms of water vapor distribution.

## 1. Introduction

A synthetic aperture radar (SAR) image contains information on the path length between the radar antenna and the resolution cells on earth. The interferometric combination of two radar images with a temporal separation of 1 day provides a sensitive tool to measure these path length differences at a fraction of the radar wavelength, which is 5.66 cm for C-band radar, used here. Conventionally, path length differences can be attributed either to topographic height differences, depending on the relative positions of the satellites (Zebker and Goldstein 1986), or to surface deformation, de-

pending on the time interval between the two observations (Gabriel et al. 1989; Massonnet et al. 1993, 1995). However, effective path length variations are also caused by radar signal delay variability within the imaged area, due to the heterogeneous refractivity distribution in the atmosphere. Signal delay, in seconds, is equivalent to an excess path length by multiplication with the speed of light in a vacuum. The excess path length can be directly obtained by integrating over the (dimensionless) refractivity along the line of sight. Over small spatial scales, the variation in the integrated refractivity is mainly due to the spatial variation of water vapor during the two image acquisitions. To a lesser extent, temperature, liquid water, and pressure gradients influence the delay variation (Hanssen et al. 1999).

Delay measurements observed by space–geodetic techniques such as the Global Positioning System (GPS) and radar interferometry (InSAR) can be used to derive precipitable water vapor in the atmosphere (Saastamo-

*Corresponding author address:* Dr. Ramon F. Hanssen, DEOS, Delft University of Technology, Thijsseweg 11, 2629 JA Delft, Netherlands.
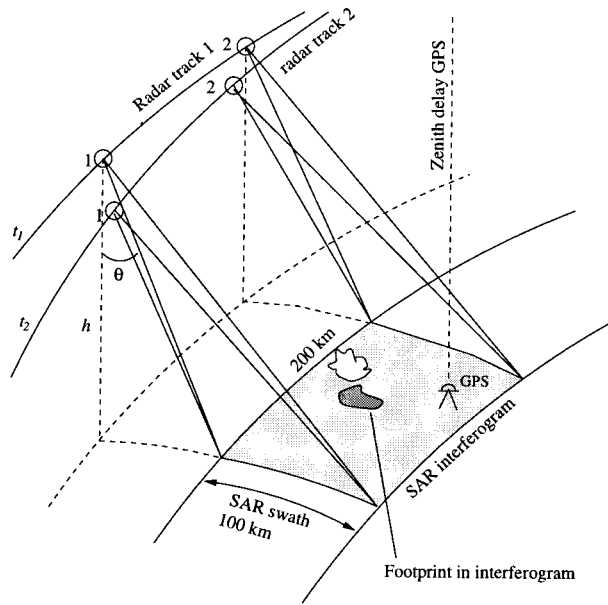E-mail: hanssen@geo.tudelft.nl

FIG. 1. Geometric configuration of the radar acquisitions. The SAR image is observed from satellite observations between points 1 and 2 of track 1 at $t_1$. The same area is viewed from track 2 at $t_2$. The mean look angle $\theta$ is approximately 21°, and the satellite height $h = 785$ km for ERS. A localized heterogeneity in the refractivity during one of the two observations will result in an increased signal delay for the corresponding footprint in the SAR image. A GPS receiver can be used to derive the zenith delay at that point during the SAR acquisition, based on slant delays to a number of GPS satellites.

inen 1972; Hogg et al. 1981). Precipitable water vapor is the amount of vertically integrated water vapor and can be expressed in kilograms per square meter or, as the height of an equivalent column of liquid water, in meters. GPS measurements provide temporal variations in precipitable water vapor at one position (see e.g., Bevis et al. 1992). Using InSAR, the data reflect spatial variations in precipitable water vapor during the two image acquisitions. Figure 1 shows the geometric configuration of the radar acquisition and the GPS zenith measurement.

Although InSAR and GPS have the same sensitivity to tropospheric refractivity variations, the validation of the InSAR images using a single GPS receiver at a fixed location only holds for one point in the image. Ideally, the validation of the InSAR results is performed using comparable image data. Unfortunately, conventional imaging radiometers do usually not provide quantitative measures for water vapor content over the entire tropospheric column and lack in spatial resolution (Weldon and Holmes 1991).

For the specific atmospheric situation studied here, with relatively transparent air, it is investigated whether accurate precipitable water vapor values can be retrieved from Meteosat radiometer observations at 6.7 $\mu$m [water vapor (WV) channel] at a local pixel resolution of 5 km × 9 km. Corresponding values of precipitable water vapor derived from a GPS ground station are used to

obtain a parameterization of the relation between the Meteosat WV brightness temperatures and precipitable water vapor.

The objective of this paper is to present the technique of integrated refractivity measurements with InSAR, introduced by Hanssen et al. (1999), in more detail and to discuss the interpretation of a SAR interferogram acquired in March 1996 in terms of precipitable water vapor distribution. Second, it is investigated whether it is possible, for this specific situation, to obtain a parameterization of radiometer brightness temperatures as a function of precipitable water vapor, using Meteosat observations and GPS time series. After establishing such a relationship for a single point, it is extended spatially to derive precipitable water vapor that can be used for validating the SAR interferogram.

In section 2, the basic principles of SAR interferometry are addressed, equations needed for the analysis of the signal delay in terms of integrated refractivity are derived, and some basic characteristics of the Meteosat observations are described. As the application and analysis of radiometer observations such as the Meteosat WV channel are well understood, the radar techniques are emphasized. Section 3 describes the methodology to derive precipitable water vapor estimates, and presents the main results of this study. Discussion and conclusions make up section 4.

## 2. Background

### a. SAR interferometry

The SAR of the European Remote Sensing Satellites (*ERS-1* and *ERS-2*) provides an amplitude and a phase value for every resolution cell of approximately 4 m × 20 m. Information on the path length between the radar antenna and a ground resolution cell is contained in the phase measurement. Unfortunately, the phase observation $\psi_p^{t_i}$ of resolution cell $p$ in an SAR acquisition at $t_i$ is a superposition of a number of contributions:

$$\psi_p^{t_i} = \psi_{p,\text{geom}}^{t_i} + \psi_{p,\text{prop}}^{t_i} + \psi_{p,\text{scat}}^{t_i}, \quad -\pi \leq \psi < \pi, \quad (1)$$

where $\psi_{p,\text{geom}}^{t_i}$ is related to the geometric distance and $\psi_{p,\text{prop}}^{t_i}$ to the signal propagation velocity variations. Most important, the scattering component, $\psi_{p,\text{scat}}^{t_i}$, is the contribution of many arbitrary scatterers in the resolution cell, which add up to produce a uniform probability density function for $\psi_{p,\text{scat}}^{t_i}$. As a consequence, the sum of the pdf's of all components in Eq. (1) will have a uniform distribution as well, and no useful phase information can be obtained.

In the interferometric combination, two SAR images, acquired at different times, are accurately aligned and differenced, which yields the interferometric phase

$$\phi_p = \psi_p^{t_1} - \psi_p^{t_2}, \quad -\pi \leq \phi < \pi, \quad (2)$$

consisting of a differenced geometric component $\phi_{p,\text{geom}}$, propagation component $\phi_{p,\text{prop}}$, and scattering

component $\phi_{p,\text{scat}}$. If the second satellite orbit is sufficiently close ($<$500 m) to the first and the physical scattering characteristics remain constant ($\psi_{p,\text{scat}}^{t_1} \approx \psi_{p,\text{scat}}^{t_2}$), the scattering component in each interferometric phase observation will be eliminated in the differencing. In that case, useful information may be obtained from the resulting difference phase image or interferogram. The assumption of a stationary scattering component is the limiting factor for the application of SAR interferometry. For example, over water or rapidly changing surfaces it is not possible to obtain coherent phase observations. Over many agricultural areas, as in the test site in this study, phase noise increases with increasing time intervals or after anthropogenic activities (see, e.g., Usai and Klees 1999). During the *ERS-1* and *ERS-2* "tandem mission," which lasted from August 1995 to April 1996, SAR images were acquired with a repeat period of 24 h. This short time interval ensures a sufficiently high correlation between consecutive acquisitions over most land surfaces.

In order to analyze the propagation component of the interferogram, the influence of the geometric component needs to be eliminated. Geometric phase differences are caused by either a change in satellite position or a coherent change in the position of the scatterers on earth, between the two acquisitions. A difference in satellite positions will measure topographic height variation in the SAR image. Using a reference elevation model, a synthetic topographic interferogram can be constructed, which can be subtracted from the observed interferogram, resulting in a so-called differential, topographic-free, interferogram (Massonnet et al. 1993). Other variations in the geometric component, for example, due to surface deformation, can be safely ignored for these short time intervals. Therefore, observed phase gradients in the differential interferogram can only be attributed to propagation delay variability and residual trends due to the inaccuracy of the satellite position during the acquisitions. Finally, the interferometric phase, which is originally "wrapped" to the interval $[-\pi, \pi]$, is unwrapped using dedicated phase-unwrapping algorithms (see, e.g., Goldstein et al. 1988).

### b. Interferometric delay analysis

After obtaining the differential interferogram, the observed phase differences can be interpreted as (i) the spatial delay variation between the radar antenna and millions of pixels in the interferogram and (ii) the difference between the two generally uncorrelated states of the atmosphere during the SAR acquisitions. Due to satellite orbit errors and the wrapped nature of the phase observations it is only possible to measure the lateral variation of the delay, rather than the total delay. The delay variation (in mm) $\delta_{p,q} = \delta_p - \delta_q$ between pixel $p$ and $q$ is directly related to the interferometric phase difference $\phi_{p,q} = \phi_p - \phi_q$ by (Hanssen 1998):

$$\delta_{p,q} = \frac{\lambda}{4\pi}\phi_{p,q} = 28\frac{\phi_{p,q}}{2\pi}. \tag{3}$$

Mapping the incidented delay variation to zenith values can be achieved by

$$\delta_{p,q}^z = \delta_{p,q}\cos\theta, \tag{4}$$

with look angle $\theta$ varying between 19° and 23° (see Fig. 1). Such a simple mapping function is sufficiently accurate for steep incidence angles (Bean and Dutton 1968).

The standard deviation $\sigma_\phi$ is derived from the coherence $\gamma$, that is, the amount of correlation between the two SAR images, with $0 \leq \gamma \leq 1$ (see Just and Bamler 1994). For $\gamma \geq 0.8$, as observed in the interferogram used in this study, we find $\sigma_\phi \leq 52°$. Using Eqs. (3) and (4), and averaging five pixels to obtain 20 m $\times$ 20 m resolution cells yields a formal accuracy of the zenith delay (vertically integrated refractivity) observations of $\sigma_{\delta^z} \approx 2$ mm. Additional spatial averaging to a ground resolution of approximately 160 m $\times$ 160 m yields a phase standard deviation of $\sigma_\phi \leq 5°$ (Joughin and Winebrenner 1994) and, consequently, $\sigma_{\delta^z} \leq 0.2$ mm.

Possible systematic errors in these delay observations are manifested as long wavelength gradients in the interferogram, caused by inaccuracies in the satellite's position during image acquisition. These additional tilts are removed from the interferogram before analyzing the delay differences. This procedure also removes long wavelength delay gradients caused by pressure and temperature gradients or gradients in ionospheric electron density.

The technique now reveals incidented delay differences or integrated refractivity along every path between the antenna position, $a$, and the resolution cells on earth. The relation between zenith delay observed at resolution cells $p$ and $q$ and the refractivity distribution during SAR acquisition $t_i$ can be written as

$$\delta_{p,q}^{z,t_i} = 2 \times 10^{-6}\cos\theta\left(\int_p^a N\,dz - \int_q^a N\,dz\right), \tag{5}$$

where $N(x, y, z, t)$ is the dimensionless refractivity. The zenith delay variation $\delta_{p,q}^z$ observed in the interferogram can be defined as

$$\delta_{p,q}^z = \delta_{p,q}^{z,t_1} - \delta_{p,q}^{z,t_2}. \tag{6}$$

For C-band radar and the location of the test site the refractivity can be written as (Smith and Weintraub 1953; Kursinski 1997; Hanssen 1998)

$$N = k_1\frac{P}{T} + \left(k_2'\frac{e}{T} + k_3\frac{e}{T^2}\right) - 4.03 \times 10^7\frac{n_e}{f^2} + 1.4W, \tag{7}$$

where $P$ is the total atmospheric pressure in hPa, $T$ is the atmospheric temperature in kelvins, $e$ is the partial

pressure of water vapor in hPa, $n_e$ is the electron number density per cubic meter, $f$ is the radar frequency (5.3 GHz), and $W$ is the liquid water content in g m$^{-3}$. The terms $k_1 = 77.6$, $k'_2 = 23.3$, and $k_3 = 3.75 \times 10^5$ are obtained from Smith and Weintraub (1953), but results from Thayer (1974) are also commonly used. The four terms are referred to as hydrostatic term, wet term, ionospheric term, and liquid term, respectively. Resch (1984) indicated that the first two parts are accurate to 0.5%.

It is obvious that the inverse problem, the retrieval of all atmospheric parameters in four dimensions from a nearly vertically integrated measurement, is ill posed. However, there are several considerations that make a reasonable interpretation of the signal delay in terms of the wet term (integrated water vapor) likely.

- *The sensitivity of the delay differences to variations in the atmospheric parameters.* Under standard atmospheric conditions, a change in surface pressure of 1 hPa will result in a 2.3-mm delay difference, whereas a small variation in moisture of 1 g kg$^{-1}$ (1.2 hPa) at 0°C already produces 6 mm per vertical kilometer. The sensitivity for a change in temperature of 1°C is 4–20 times smaller than a change in moisture of 1 hPa, depending on ambient conditions. The influence of cloud droplets is maximally a few millimeters, depending on the droplet size and cloud height. Ice crystal influence can be neglected for 5.66-cm radar wavelengths (Hanssen et al. 1999).

- *The dominant spatial wavelengths of the variations.* For example, the influence of the hydrostatic term depends on the spatial variation of surface pressure within a 100 km × 100 km SAR image. For most meteorological situations, this variation can be approximated by a single gradient. For the ionospheric term, similar reasoning holds in most cases for latitudes studied here. Moisture variations, however, of 1 g kg$^{-1}$ are common even on a 1-km spatial scale and will have a directly noticeable effect in the interferogram (Weckwerth et al. 1997).

- *Assumptions on vertical stratification and topographic effects.* As long as the vertical variation of atmospheric parameters is identical for every resolution cell in the interferogram, these effects will not influence the interferometric phase. Note that a different vertical layering during the two SAR acquisitions will, however, influence the interferogram if significant topography is present (Delacourt et al. 1998; Hanssen and Klees 1999). The signatures of these effects will have strong correlation with the topography. For the test site analyzed here, with height variation within a range of 100 m, no topographic induced effects are expected or observed.

### c. Meteosat water vapor channel

The Meteosat WV channel, centered around 6.7 $\mu$m, is used in operational meteorology to observe the de-

velopment of structures of upper-tropospheric water vapor, which carry the signatures of atmospheric conditions. Especially subsidence inversions, that is, downward vertical transport of dry air behind a frontal zone, are clearly visible in the WV images. Due to the strong absorption by water vapor at this wavelength, the observed brightness temperatures usually originate from tropospheric layers above 3 km (Weldon and Holmes 1991). Therefore, quantitative analysis is restricted to upper-tropospheric water vapor as described by Schmetz et al. (1995). Unfortunately, however, the concentration of water vapor is highest near the earth's surface, where relatively high pressure and temperature allow the air to contain more water vapor. Therefore, in general it is not possible to make one unique parameterization of WV channel brightness temperatures into precipitable water vapor. In section 3b it is discussed whether GPS tropospheric delay time series are suitable for establishing a tailor-made parameterization to obtain Meteosat spatial precipitable water vapor values for the special case of a subsidence inversion.

## 3. Methodology and results

### a. SAR interferogram analysis

An interferogram, covering a strip of 100 km × 200 km, has been formed using SAR acquisitions on 26 and 27 March 1996, 2141:05 UTC (2241:05 local time). The orbital separation, parallel to the look direction, is approximately 32 m, which makes the configuration moderately sensitive to topographic height differences (see Fig. 1). An a priori reference elevation model is used to correct for the topographic phase in the interferogram (TDN/MD 1997). Some additional corrections for tilts in the length and width direction are applied, and water surfaces are masked. The resulting differential interferogram is shown in Fig. 2. The phase values are converted to zenith wet delays, using Eqs. (3) and (4), and consecutively to differential precipitable water vapor using Eq. (10), where we use the term ''differential'' to indicate the difference between the two states of the atmosphere during the SAR acquisitions.

A strong, large-scale gradient is clearly visible in the south of the interferogram, aligned approximately perpendicular to the radar flight direction. The interpretation of this phenomenon is a key topic of this study. Previous studies have shown that phase variation perpendicular to the flight direction might be caused by oscillator drift errors in the onboard reference clock (Massonnet and Vadon 1995). A possible way to examine this possibility would be the calculation of a long swath of connected SAR images, but this is outside the scope of this study. Here it is assumed that the phase variation is caused by atmospheric water vapor only. The likelihood of this assumption can be tested using the combined analysis with Meteosat and GPS.

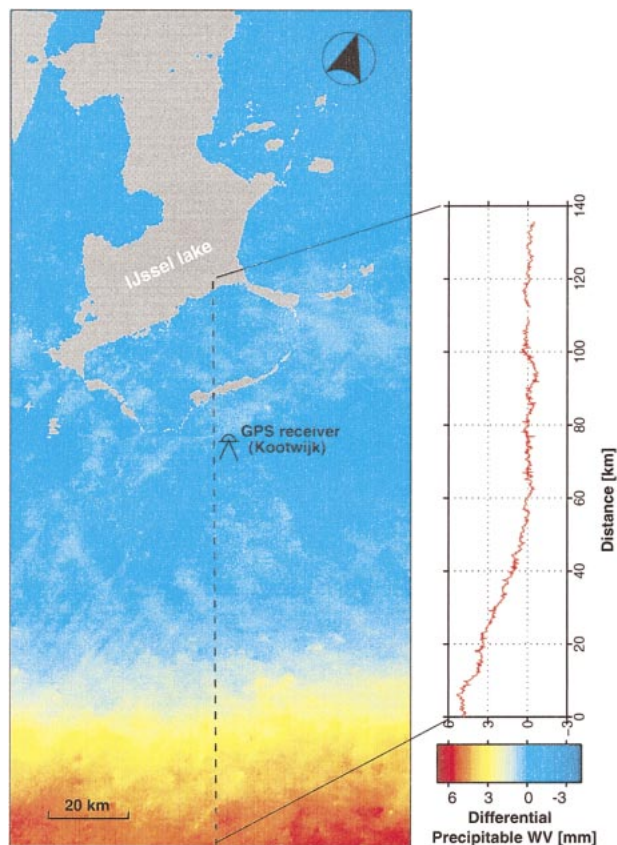Note that, apart from the gradient in the south of the

FIG. 2. The differential SAR interferogram of 2141 UTC 26 and 27 Mar 1996. The location of the interferogram in the region is indicated in Fig. 3. Interferometric phase observations are unwrapped and converted to differential precipitable water vapor—the difference between the precipitable water vapor distributions during the two acquisitions. Topographic information has been removed using a reference elevation model, and water areas are masked. The dashed line indicates the location of the analyzed profile (see Fig. 7). The location of the GPS receiver at KOSG is sketched in the figure. Diagonal waves are observed in the lower left-hand corner of the interferogram.

interferogram, wave phenomena also can be observed in the interferogram (see the lower left-hand part of Fig. 2). These are possibly due to low-level moisture variations of which the structure seems to indicate the presence of boundary layer rolls.

Wet delay differences $\delta_{pq}^z$ can be related to integrated precipitable water ($I$) values, the liquid equivalent of the integrated water vapor:

$$\delta_{pq}^z = \Pi_{T_s}^{t_1}(I_p^{t_1} - I_q^{t_1}) - \Pi_{T_s}^{t_2}(I_p^{t_2} - I_q^{t_2}). \quad (8)$$

Using the density of liquid water, we find that 1 mm integrated precipitable water is equal to 1 kg m$^{-2}$ integrated water vapor. The conversion factor $\Pi_{T_s}^{t_i}$ is approximated using surface temperatures $T_s$ for the image acquired at $t_i$, defined by Askne and Nordius (1987). After first models for $\Pi_{T_s}^{t_i}$ were derived by Davis et al. (1985) and Bevis et al. (1994), a polynomial model was developed to approximate $\Pi_{T_s}^{t_i}$ for De Bilt, the reference

site in the Netherlands, using 1461 radiosonde profiles (Emardson and Derks 2000):

$$\Pi_{T_s, t_D}^{t_i} = a_0 + a_1(T_s - T_0) + a_2(T_s - T_0)^2$$

$$+ a_3 \sin\left(2\pi \frac{t_D}{365}\right) + a_4 \cos\left(2\pi \frac{t_D}{365}\right), \quad (9)$$

where $T_0$ is the mean annual surface temperature for the location, and $t_D$ is the day number of the year. The used coefficients are $a_0 = 6.443$, $a_1 = -1.33 \times 10^{-2}$, $a_2 = 0.18 \times 10^{-4}$, $a_3 = 3.6 \times 10^{-2}$, $a_4 = 3.0 \times 10^{-2}$, and $T_0 = 283.80$ K. Using surface temperatures provided by 18 stations in the area, we find that $1/\Pi^{t_1} = 0.1513 \pm 0.0004$ and $1/\Pi^{t_2} = 0.1507 \pm 0.0005$, for 26 and 27 March, respectively. Applying one factor for both days, $1/\Pi_m = 0.1510 \pm 0.0005$ is justified, since the fractional error in $\Pi$ is one order of magnitude smaller than the fractional error in the delay measurement. We can rewrite Eq. (8) as

$$\nabla I_{pq}^{t_1,t_2} = (I_p^{t_1} - I_q^{t_1}) - (I_p^{t_2} - I_q^{t_2}) = \Pi_m^{-1}\delta_{pq}^z, \quad (10)$$

where we define $\nabla I_{pq}^{t_1,t_2}$ as the double difference of integrated precipitable water in space and time. Note that a single, isolated anomaly will have a different sign in the interferogram, depending on whether it appeared in the first or the second acquisition. In that case, one of the single spatial $\Delta I_{pq}^{t_i}$ differences can be regarded as nearly zero, in which case we can interpret the double difference as a single spatial difference during the other acquisition.

### b. Meteosat WV channel analysis

On 27 March 1996 a strong subsidence inversion passed the Netherlands from north to south, which was clearly visible in the WV channel images (Fig. 3). The subsidence inversion can be identified by the dark band in the image, corresponding to relatively high brightness temperatures. Because the descending air in the subsidence inversion is rather dry, the absorption (and emission) of radiation is low and, therefore, the air is relatively transparent. This enables radiation from lower (warmer) layers to contribute to the signal, which results in high apparent brightness temperatures. The center of the subsidence inversion moves in one day from about 53° to 48°N, as apparent from Fig. 3.

Assuming that the brightness temperature variations in the Meteosat WV images reflect the variations of the total water vapor column, we use GPS-derived precipitable water vapor observations to parameterize the brightness temperature. The reference to the WV channel are collocated measurements from GPS ground station Kootwijk, at 52.17°N, 5.80°E (see Fig. 2). From the GPS measurements, reliable absolute values for precipitable water vapor are derived, using the standard methodology described in Bevis et al. (1992, 1994). The accuracy of the GPS-derived precipitable water vapor
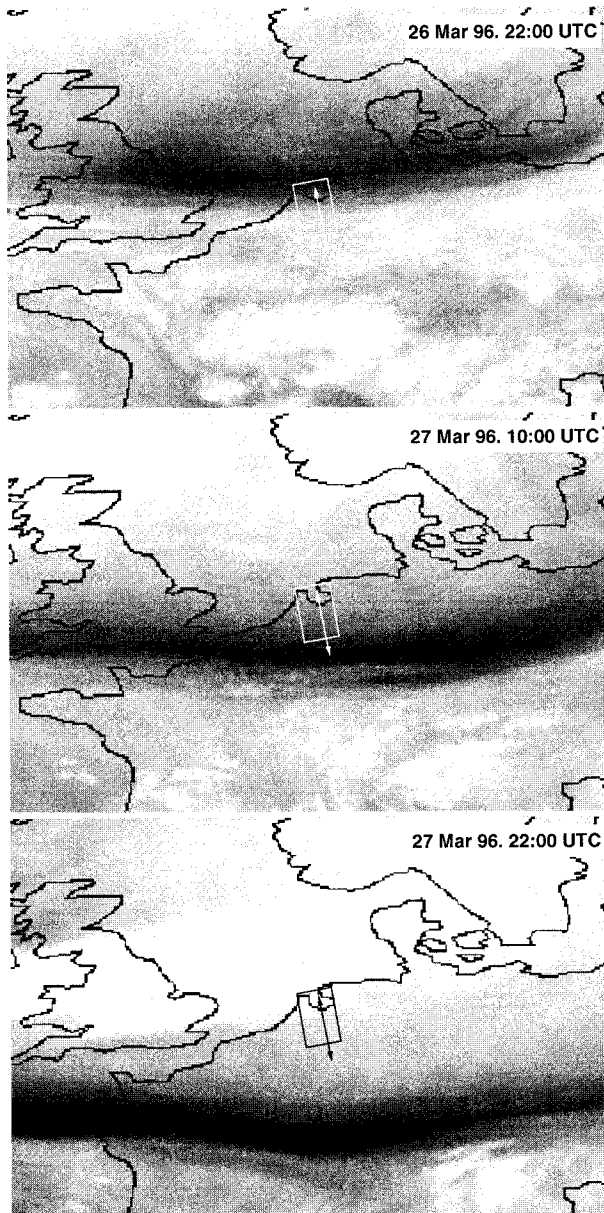
FIG. 3. Meteosat 6.7-$\mu$m water vapor images at 2200 UTC 26 Mar, and 1000 and 2200 UTC 27 Mar. Brightness temperatures range from $-50°C$ (white) to $-10°C$ (black). The interferogram area is indicated in the center of the image. The arrow indicates the range over which brightness temperatures were used for comparison with the GPS observations.

is approximately 2 mm. For 27 hourly observations of GPS precipitable water vapor and Meteosat signal intensity, shown as scatter plot in Fig. 4, the correlation can be parameterized as

$$I = 36.7 - 0.56\zeta + 0.0022\zeta^2, \qquad (11)$$

with $I$ in kilograms per square meter and $\zeta$ the signal intensity of the WV channel in number of counts. The rms value of the difference between model and observations is 0.6 kg m$^{-2}$.
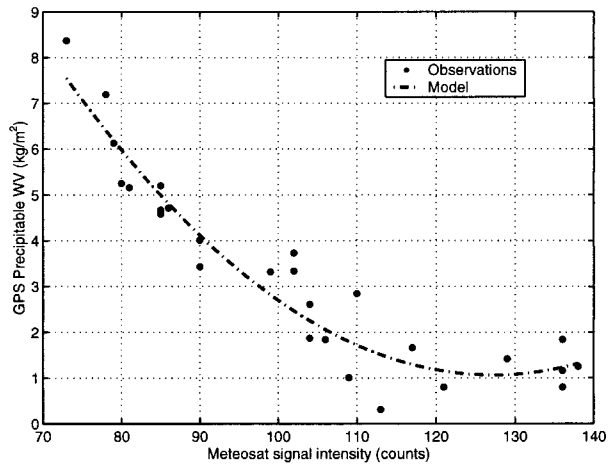


FIG. 4. Scatterplot of observed GPS precipitable water vapor and Meteosat water vapor channel signal intensity, for hourly observations between 1800 UTC 26 Mar and 2000 UTC 27 Mar. The derived polynomial is indicated by the line. The rms best least squares quadratic is 0.6 kg m$^{-2}$.

In Fig. 5 the change in $I$ over Kootwijk is shown derived from both GPS and Meteosat. We find that the rms of 0.6 kg m$^{-2}$ is accurate enough for our analysis. The passage of the subsidence inversion from north to south is clearly visible. Values range from 1 to 7 kg m$^{-2}$.

Using the parameterization in Eq. (11), precipitable water vapor can be derived from the Meteosat WV channel image. The parameterization yields accurate values for the area near Kootwijk (location indicated in Fig. 2), but with increasing distance the accuracy will probably decrease.

For the comparison with the SAR interferogram, an elongated area is selected (indicated by the arrow in Fig. 3), which ranges from 51.38°N, 5.93°E to 52.72°N, 5.43°E. The area includes the GPS station Kootwijk Observatory for Satellite Geodesy (KOSG), to optimize the validity of our parameterization, and is parallel to the ground track of ERS. The subsidence inversion band is nearly perpendicular to the profile and moves approximately parallel to it. As a result, the analyzed precipitable water vapor signal is dominated by only one atmospheric process—the subsidence inversion. There-
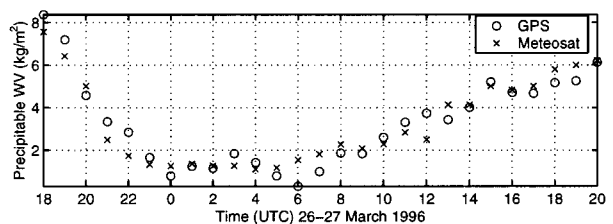


FIG. 5. Comparison of hourly precipitable water vapor over Kootwijk derived from Meteosat brightness temperature, using Eq. (11), and derived from GPS zenith delays.
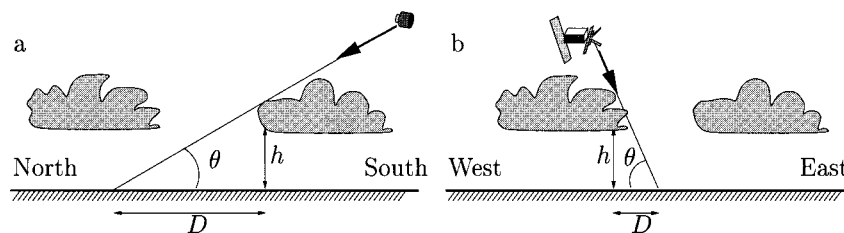
FIG. 6. Sketch of the horizontal shift of the position of water vapor due to the oblique viewing geometry of (a) Meteosat and (b) ERS. For latitude 52°N, the elevation angles $\theta$ are 30.5° for Meteosat and 69° for ERS.

fore, the parameterization is assumed to be sufficiently accurate for the selected profile.

All pixels that contain high-altitude clouds (temperature below −20°C) are excluded from the analysis, to increase the reliability of the parameterization. In a cloud, the fraction of total water that is clustered in particles is generally small, but the absorption of radiation by these particles is much larger than the absorption by the water vapor in the cloud. Therefore, the correlation between the Meteosat WV channel observations and the correct amount of precipitable water vapor will deteriorate if clouds are present.

To obtain similar quantities, as in the interferogram, the extracted profiles corresponding with 2200 UTC 26 March and 2200 UTC 27 March are differenced. The resulting values are indicated by the triangles in Fig. 7, where the position of the pixels along the profile is expressed by their latitude. From the Meteosat WV images in Fig. 3 it appears that at 2200 UTC 26 March the selected area was in the front part of the subsidence inversion, which results in a decreasing amount of precipitable water vapor with latitude. At 2200 UTC 27 March, the selected area was in the back part, resulting in an increasing amount of precipitable water vapor with latitude. As a consequence of these opposite trends, the quantities in Fig. 7—which are formed by subtracting the values at 27 March from the values at 26 March—have an amplified north–south gradient. In the next section these results will be compared with the results from SAR interferometry.

## c. Intercomparison

The evaluation of the water vapor observations from the Meteosat WV channel and the radar interferogram is subject to 5 degrees of freedom.

1) The interferogram shows relative delay differences. Therefore, the analyzed profile has an arbitrary bias when compared with the absolute values of the Meteosat profile.
2) Due to the oblique viewing geometry of the radar (23° from zenith) the profile will be shifted some kilometers parallel to the west (see Fig. 6). Since the atmospheric situation during the two acquisitions was nearly symmetric (i.e., perpendicular to the profile), the effect of this lateral shift is negligible.
3) The inaccuracy in the satellite orbits might lead to a small tilt in the profile. Here we assume that this tilt is sufficiently eliminated by using a number of reference points during preprocessing.
4) The Meteosat positioning accuracy is approximately 0.5 pixels, corresponding to a 4.5-km uncertainty in north–south direction.
5) Due to the geostationary position over the equator, there is an additional shift $D$ in north–south direction when the majority of the water vapor is at a height $h$ (see Fig. 6). In that case, the information will appear to be shifted northward in the image. For the location analyzed here, this shift is approximately $D = 1.7 \times h$. Note that the time difference between the SAR acquisition and the Meteosat scan of the latitudes of the Netherlands (13 min) might also account for a slight additional shift.

Estimates of the a priori standard deviation of both the Meteosat and InSAR precipitable water vapor estimates are needed to evaluate the correlation between the two profiles. For the Meteosat observations, $\sigma_{I,\mathrm{msat}}$, is assumed to be uncorrelated and equal for every observation. In section 3b, an rms value of 0.6 kg m$^{-2}$ was derived from a comparison with GPS observations. The analyzed profile values are differences between corresponding observations for two consecutive days. Assuming zero covariance between the two days, standard error propagation yields a priori value for $\sigma_{\Delta I,\mathrm{msat}} = 0.85$ kg m$^{-2}$.

The expected variance for the InSAR observations is assumed to be uncorrelated between adjacent values and equal for every observation. In section 2b, the delay standard deviation $\sigma_{\delta z} = 0.2$ mm (or kg m$^{-2}$) was derived. Using Eq. (10), simple error propagation yields an a priori value for the integrated water vapor observations of $\sigma_{I,\mathrm{sar}} = 0.08$ kg m$^{-2}$.

A goodness-of-fit parameter between the InSAR and the Meteosat observations can be optimized by adjusting the 5 degrees of freedom mentioned above, or by adjusting the a priori variances of both observations. Here, a combination of both approaches is suggested. Parameters 2–4 are assumed to be sufficiently well approxi-
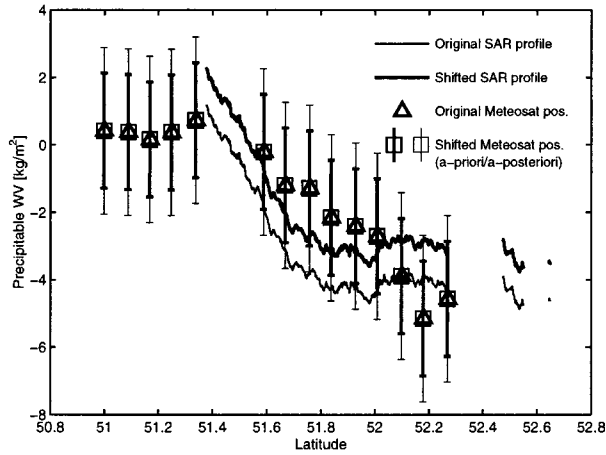
FIG. 7. Goodness-of-fit analysis, based on best $\chi_\nu^2$ value. The error bars express the scaled $2\sigma$ (95%) confidence interval based on the combined variance of the Meteosat and INSAR profile. The original (arbitrary) values of the INSAR profile are shown as the thin line, the best-fit values by the bold line. The original Meteosat positions are indicated by the triangles and the slightly shifted best-fit values by the squares. The best $\chi_\nu^2$ value is obtained by scaling the a priori variances (bold inner error bars) with factor 1.44, resulting in the thin outer error bars.

mated. A northward shift of the Meteosat observations (parameter 5) of 5 km is used as a first-order approximation, derived from an average height of the dominant water vapor signal in the WV channel. The additional Meteosat profile shift, the bias of the InSAR profile (parameter 1), and the scaling factor for the variances are now estimated by deriving the minimal reduced chi-square value, $\chi_\nu^2$, of the two profiles as a function of the bias of the InSAR profile (Bevington and Robinson 1992):

$$\chi_\nu^2 = \frac{1}{n-1} \sum_{i=1}^{n} \left( \frac{r_i}{\sigma_i} \right)^2. \qquad (12)$$

The number of measurements is denoted by $n$, $r_i$ are the differences between the Meteosat and the INSAR profile values, and $\sigma_i$ are the a priori standard deviations of the differences, that is, $\sigma_i^2 = \sigma_{I,\text{sar},i}^2 + \sigma_{\Delta I,\text{msat},i}^2$. Here we find $\sigma_i = 0.85$ kg m$^{-2}$ for all $i \in [1, \ldots, n]$. Note that the contribution of $\sigma_{\Delta I,\text{msat},i}$ is one order of magnitude larger than $\sigma_{I,\text{sar},i}$.

The $\chi_\nu^2$ values are expressed as a function of the InSAR profile bias and the horizontal shift of the Meteosat profile. The search window of the bias has been confined between $-3$ and 3 kg m$^{-2}$, whereas the horizontal shift is confined between $-1.1$ and 1.1 km. The minimum value, $\chi_\nu^2 = 2.1$, is found for a bias of 1 kg m$^{-2}$ and a horizontal shift of $-1.1$ km. Figure 7 shows the original position of the InSAR profile, indicated by the thin line, and the new position, indicated by the bold line. The original position of the Meteosat profile values is indicated by the triangles, while the new positions are indicated by the squares. A 95% confidence interval for the difference of the two data sources is indicated

by the inner error bars. Note that the error bars are drawn at the Meteosat positions, although they also include a small component of the InSAR profile.

From this evaluation it is clear that the adjustment of the free parameters is not sufficient to reach a satisfying comparison. The estimated variance $\hat{\sigma}^2$ can be approximated by (Bevington and Robinson 1992)

$$\hat{\sigma}^2 = \chi_\nu^2 \sigma_i^2, \qquad (13)$$

if all variances $\sigma_i^2$ are equal. If both profiles describe the same physical process, the estimated variance should agree well with the a priori variance and the value of the reduced chi-squared should be approximately unity. In order to reach this situation, the a priori standard deviations of the difference need to be scaled by a factor $\sqrt{\chi_\nu^2} = 1.44$. This implies that the a priori standard deviation of the difference has been too optimistic. An a posteriori standard deviation of 1.23 mm is found, indicated in Fig. 7 by the outer error bars.

## 4. Conclusions

Satellite radar interferometry can be applied to study vertically integrated atmospheric refractivity variations with a spatial resolution of 20 m and an accuracy of 2 mm, irrespective of cloud cover or solar illumination. Although satellite repeat acquisitions are still far to sparse for operational meteorology, the technique can currently be used for studying mesoscale atmospheric dynamics and provides new insights, particularly in mapping the small-scale water vapor distribution. This study elaborates on the main principles and limitations.

For a specific atmospheric situation in March 1996, precipitable water vapor obtained from SAR interferometry is validated by GPS time delay analyses combined with Meteosat 6.7-$\mu$m WV channel observations. The interferometric phase observations are converted to relative signal delay observations and consecutively processed to precipitable water vapor. For a point location, Meteosat brightness temperature time series are converted to precipitable water vapor using a parameterization obtained from GPS wet signal delay observations. Applying this parameterization spatially for a profile of brightness temperatures in two WV channel images, acquired at nearly the same time as the two SAR images, enables a direct comparison between the two sources.

The results show that the phase gradient observed in the SAR interferogram is fully accounted for by a subsidence inversion that moved over the interferogram area during the two SAR acquisitions. The subsidence inversion resulted in temporal precipitable water vapor variations over a range of approximately 6 kg m$^{-2}$, as observed by GPS and Meteosat. Accounting for the relative character of the InSAR observations, and the positioning uncertainty of the Meteosat images, both datasets describe the same phenomenon in a minimal reduced chi-squared sense with 1.23 kg m$^{-2}$ standard de-

viation. Because the range of the signal encompasses approximately 6 kg m$^{-2}$, signal-to-noise ratio values are sufficient to identify the same signal in both data sources. This supports the statement that radar interferometry can be used to derive the spatial variations in precipitable water vapor.

Although the parameterization used in Eq. (11) appears to be sufficient to explain the observations, it needs to be stressed that the use of this method is feasible only for a limited area around the GPS receiver. Moreover, in situations with severe cloud cover, the conversion from brightness temperatures to precipitable water vapor is not likely to succeed, due to insufficient penetration caused by absorption. Future applications of the technique need to be focused on consecutive acquisitions of SAR images in order to obtain ''cascade'' series of interferograms. Such approaches can result in resolving the ambiguity between the atmospheric states during the two acquisitions.

## REFERENCES

Askne, J., and H. Nordius, 1987: Estimation of tropospheric delay for microwaves from surface weather data. *Radio Sci.,* **22,** 379–386.

Bean, B. R., and E. J. Dutton, 1968: *Radio Meteorology.* Dover, 435 pp.

Bevington, P. R., and D. K. Robinson, 1992: *Data Reduction and Analysis for the Physical Sciences.* 2d ed. McGraw-Hill, 328 pp.

Bevis, M., S. Businger, T. A. Herring, C. Rocken, R. A. Anthes, and R. H. Ware, 1992: GPS meteorology: Remote sensing of atmospheric water vapor using the Global Positioning System. *J. Geophys. Res.,* **97,** 15 787–15 801.

——, ——, ——, R. A. Anthes, C. Rocken, and R. H. Ware, 1994: GPS meteorology: Mapping zenith wet delays onto precipitable water. *J. Appl. Meteor.,* **33,** 379–386.

Davis, J. L., T. A. Herring, I. I. Shapiro, A. E. E. Rogers, and G. Elgered, 1985: Geodesy by radio interferometry: Effects of atmospheric modelling errors on estimates of baseline length. *Radio Sci.,* **20,** 1593–1607.

Delacourt, C., P. Briole, and J. Achache, 1998: Tropospheric corrections of SAR interferograms with strong topography: Application to Etna. *Geophys. Res. Lett.,* **25,** 2849–2852.

Emardson, T. R., and H. J. P. Derks, 2000: On the relation between the wet delay and the integrated precipitable water vapour in the European atmosphere. *Meteor. Appl.,* **7,** 61–68.

Gabriel, A. K., R. M. Goldstein, and H. A. Zebker, 1989: Mapping small elevation changes over large areas: Differential radar interferometry. *J. Geophys. Res.,* **94,** 9183–9191.

Goldstein, R. M., H. A. Zebker, and C. L. Werner, 1988: Satellite radar interferometry: Two-dimensional phase unwrapping. *Radio Sci.,* **23,** 713–720.

Hanssen, R., 1998: *Atmospheric Heterogeneities in Tandem SAR Interferometry.* Delft University Press, 136 pp.

——, and R. Klees, 1999: An empirical model for the assessment of DEM accuracy degradation due to vertical atmospheric stratification. *Proc. Second Int. Workshop on ERS SAR Interferometry, 'FRINGE99',* Liège, Belgium, European Space Agency, 1–5.

——, T. M. Weckwerth, H. A. Zebker, and R. Klees, 1999: High-resolution water vapor mapping from interferometric radar measurements. *Science,* **283,** 1295–1297.

Hogg, D. C., F. O. Guiraud, and M. T. Dekker, 1981: Measurement of excess radio transmission length on earth–space paths. *Astron. Astrophys.,* **95,** 304–307.

Joughin, I. R., and D. P. Winebrenner, 1994: Effective number of looks for a multilook interferometric phase distribution. *Int. Geoscience and Remote Sensing Symp.,* Pasadena, CA, GRSS, 2276–2278.

Just, D., and R. Bamler, 1994: Phase statistics of interferograms with applications to synthetic aperture radar. *Appl. Opt.,* **33,** 4361–4368.

Kursinski, E. R., 1997: The GPS radio occultation concept: Theoretical performance and initital results. Ph.D. thesis, California Institute of Technology, 370 pp.

Massonnet, D., and H. Vadon, 1995: ERS-1 internal clock drift measured by interferometry. *IEEE Trans. Geosci. Remote Sens.,* **33,** 401–408.

——, M. Rossi, C. Carmona, F. Adagna, G. Peltzer, K. Feigl, and T. Rabaute, 1993: The displacement field of the Landers earthquake mapped by radar interferometry. *Nature,* **364,** 138–142.

——, P. Briole, and A. Arnaud, 1995: Deflation of Mount Etna monitored by spaceborne radar interferometry. *Nature,* **375,** 567–570.

Resch, G. M., 1984: Water vapor radiometry in geodetic applications. *Geodetic Refraction,* by F. K. Brunner, Ed., Springer-Verlag, 53–84.

Saastamoinen, J., 1972: Introduction to practical computation of astronomical refraction. *Bull. Geod.,* **106,** 383–397.

Schmetz, J., and Coauthors, 1995: Monthly mean large-scale analyses of upper-tropospheric humidity and wind field divergence derived from three geostationary satellites. *Bull. Amer. Meteor. Soc.,* **76,** 1578–1584.

Smith, E. K., Jr., and S. Weintraub, 1953: The constants in the equation for atmospheric refractive index at radio frequencies. *Proc. Inst. Radio Eng.,* **41,** 1035–1037.

TDN/MD, 1997: TopHoogteMD digital elevation model. Topografische Dienst Nederland and Meetkundige Dienst Rijkswaterstaat.

Thayer, G. D., 1974: An improved equation for the radio refractive index of air. *Radio Sci.,* **9,** 803–807.

Usai, S., and R. Klees, 1999: SAR interferometry on very long time scale: A study of the interferometric characteristics of man-made features. *IEEE Trans. Geosci. Remote Sens.,* **37,** 2118–2123.

Weckwerth, T. M., J. W. Wilson, R. M. Wakimoto, and N. A. Crook, 1997: Horizontal convective rolls: Determining the environmental conditions supporting their existence and characteristics. *Mon. Wea. Rev.,* **125,** 505–526.

Weldon, R. B., and S. J. Holmes, 1991: Water vapor imagery interpretation and applications to weather analysis and forecasting. NOAA Tech. Rep. NESDIS 57, 213 pp.

Zebker, H. A., and R. M. Goldstein, 1986: Topographic mapping from interferometric synthetic aperture radar observations. *J. Geophys. Res.,* **91,** 4993–4999.